CHEMISTRY

Alkylperoxy radicals are responsible for the formation of oxygenated primary organic aerosol

Omar El Hajj[1], Samuel W. Hartness[1], Gregory W. Vandergrift[2], Yensil Park[3], Chase K. Glenn[1], Anita Anosike[1], Annabelle R. Webb[4], Nicholas S. Dewey[4], Anna C. Doner[4], Zezhen Cheng[2], Gurneesh S. Jatana[3], Melanie Moses-DeBusk[3], Swarup China[2], Brandon Rotavera[1,4]*, Rawad Saleh[1]*

Organic aerosol (OA) is an air pollutant ubiquitous in urban atmospheres. Urban OA is usually apportioned into primary OA (POA), mostly emitted by mobile sources, and secondary OA (SOA), which forms in the atmosphere due to oxidation of gas-phase precursors from anthropogenic and biogenic sources. By performing coordinated measurements in the particle phase and the gas phase, we show that the alkylperoxy radical chemistry that is responsible for low-temperature ignition also leads to the formation of oxygenated POA (OxyPOA). OxyPOA is distinct from POA emitted during high-temperature ignition and is chemically similar to SOA. We present evidence for the prevalence of OxyPOA in emissions of a spark-ignition engine and a next-generation advanced compression-ignition engine, highlighting the importance of understanding OxyPOA for predicting urban air pollution patterns in current and future atmospheres.

INTRODUCTION

Atmospheric aerosols exhibit profound impacts on air quality and the climate. Commonly referred to as particulate matter (PM) in the public-health community, aerosols are associated with various health effects and inflict the highest social cost among air pollutants (*1*, *2*). Unlike greenhouse gases, which perturb the atmospheric radiative balance via a straightforward mechanism (the greenhouse gas effect), aerosols exhibit complex direct and indirect interactions with atmospheric radiation, rendering them the largest contributor to uncertainty in climate calculations (*3*). Organic aerosol (OA) constitutes the majority of submicron aerosol mass in both urban and rural atmospheres (*4*). A large fraction of OA forms via diverse gas-phase chemical reaction pathways that produce molecules with low volatilities, favoring particle formation via condensation. These reactions occur during combustion (*5*), leading to the formation of primary OA (POA), as well as in the atmosphere (*6*, *7*), leading to the formation of secondary OA (SOA). Although OA mass concentrations in the atmosphere can be quantified with relatively high confidence, detailed speciation of OA is challenging. In response, atmospheric chemists have devised creative techniques that allow grouping OA into different categories and linking these categories to sources (*4*). The most prevalent categorization framework is based on factor analysis applied to aerosol mass spectrometer measurements (*8*, *9*). In this framework, hydrocarbon-like OA (HOA) represents OA with low oxygen content (O/C < 0.1), while oxygenated OA (OOA) represents OA with high oxygen content (0.25 < O/C < 1). The current consensus is that OOA is predominantly composed of SOA, while urban POA, emitted from the combustion of hydrocarbon fuels (e.g., vehicle emissions), is HOA (*4*). Here, we show that hydrocarbon combustion can emit what we refer to as oxygenated POA (OxyPOA), which retains chemical properties similar to those of SOA. We present results from laboratory experiments that link OxyPOA formation to low-temperature combustion (LTC) chemistry (*10*–*12*). We also provide evidence of OxyPOA in emissions from spark-ignition and next-generation advanced compression-ignition engines, illustrating the relevance of elucidating OxyPOA formation to understanding OA pollution in current and future urban atmospheres.

RESULTS

Difference in POA emitted from first-stage and second-stage ignition

Figure 1 shows results from chemical analysis of POA emitted from the controlled combustion of *n*-pentane and *n*-heptane. We distinguish between "first-stage POA," which formed at relatively low temperatures (550 to 650 K) where reactions of peroxy radicals (RO_2) dominate, and "second-stage POA," which formed at relatively high temperatures (>1000 K) (see fig. S1). Traditionally, only second-stage POA has been thought to constitute POA emissions from the combustion of hydrocarbon fuels, whereas first-stage POA was only recently found (*13*). Therefore, it is imperative to set the appropriate context for the results. Second-stage POA forms at relatively high temperatures (>1000 K) and is equivalent to "incipient soot" in combustion science terminology (*14*). It is composed of polycyclic aromatic hydrocarbons (PAHs) and aliphatic species (*5*) and therefore falls strictly under HOA (*4*). With further increase in temperature, the organic molecules that comprise second-stage POA transform into mature soot (*14*), which is largely equivalent to black carbon (BC) in atmospheric science terminology (*15*). BC is a strong light absorber and a leading contributor to global warming (*15*). Second-stage POA can also be light absorbing and is categorized as brown carbon (*16*). For these reasons, the formation and physicochemical properties of second-

[1]School of Environmental, Civil, Agricultural, and Mechanical Engineering, University of Georgia, Athens, GA 30602, USA. [2]Pacific Northwest National Laboratory, Richland, WA 99352, USA. [3]Energy and Transportation Science Division, Oak Ridge National Laboratory. Oak Ridge, TN 37831, USA. [4]Department of Chemistry, University of Georgia, Athens, GA 30602, USA.
*Corresponding author. Email: rawad@uga.edu (R.S.); rotavera@uga.edu (B.R.)

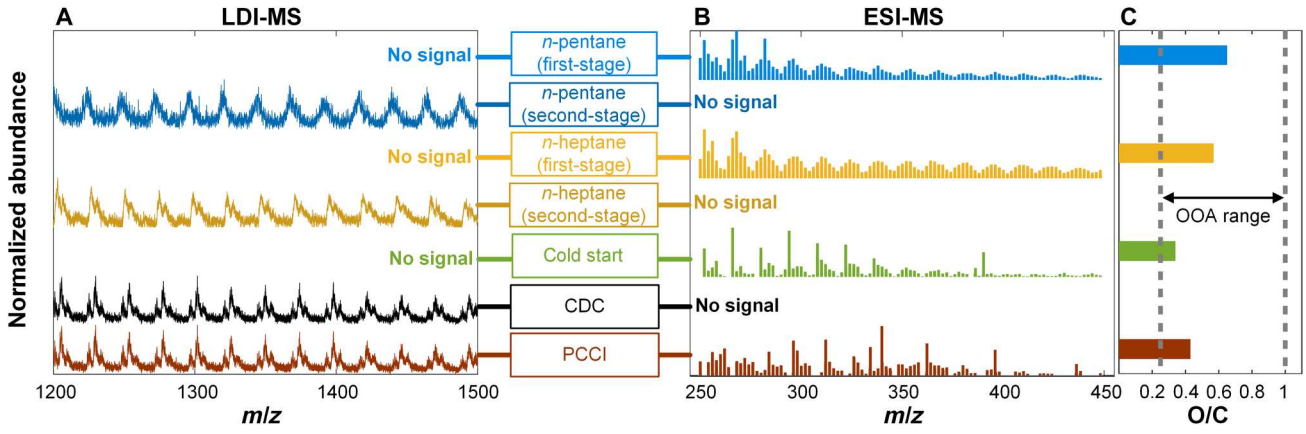

Fig. 1. Mass spectrometry analysis of POA emissions from controlled combustion of *n*-pentane and *n*-heptane, a spark-ignition engine operated at simulated cold-start conditions, and a compression-ignition engine operated at steady-state conditions using either conventional diesel combustion strategy or an ACI strategy (premixed charge compression ignition). The temperature of the *n*-pentane and *n*-heptane combustion was controlled to emit either first-stage POA (550 to 650 K) or second-stage POA (1100 to 1300 K) (see the Supplementary Materials). (**A**) Mass spectra obtained using LDI-MS. (**B**) Mass spectra obtained using ESI-MS. (**C**) Average O/C of the molecules detected by ESI-MS. The *n*-heptane first-stage POA was also analyzed using high-resolution nanospray desorption electrospray ionization (nano-DESI) MS, which yielded mass spectra and average O/C (0.57) consistent with ESI-MS (fig. S3). CDC, conventional diesel combustion; PCCI, premixed charge compression ignition; *m/z*, mass/charge ratio.

stage POA have been extensively studied by both combustion scientists and atmospheric scientists (*5*, *13*, *16*, *17*).

Some hydrocarbon fuels, including *n*-pentane and *n*-heptane, exhibit two-stage ignition behavior (*18*, *19*), with first-stage ignition occurring at relatively low temperatures (550 to 750 K). Discovery of first-stage ignition in the mid-20th century was motivated by efforts to understand the cause of engine knock in spark-ignition engines (*20*, *21*). Furthermore, the importance of first-stage ignition in advanced compression-ignition (ACI) engines that rely on LTC remains an impetus for unveiling chemical kinetics of RO_2. As part of a complex degenerate chain-branching mechanism, RO_2 isomerization to (carbon-centered) QOOH radicals and subsequent reactions are the focal points for understanding chain-branching reactions in combustion (*12*, *22*). However, while the dynamics of two-stage ignition chemistry is known to rely on QOOH-mediated reactions below 1000 K, the concomitant production of organic molecules with volatilities low enough to condense and form OA (i.e., first-stage POA) has only recently been reported (*13*).

The second-stage POA generated in our experiments was detected by laser desorption ionization mass spectrometry (LDI-MS) and exhibited clusters of peaks separated by 12 u (fig. S2), which are characteristic signatures of PAHs. Similar spectra have been reported for POA extracted from flames (*23*, *24*) and pyrolysis of hydrocarbons (*25*, *26*). The clusters of peaks with 12-u separation have been shown to correspond to two series associated with even carbon numbers (usually major peaks) and odd carbon numbers (usually minor peaks), each separated by 24 u, with 12-u offset between them. At large molecular sizes, the minor peaks become less prominent and can disappear from the spectra (*16*, *24*, *27*), leaving the major peaks with 24-u separation (Fig. 1).

Being nonpolar, the second-stage POA molecules were not efficiently ionized by electrospray ionization (ESI) and were thus not detected by ultrahigh-resolution ESI-MS. Conversely, the first-stage POA was transparent to LDI-MS but was detected by ESI-MS, indicating that the first-stage POA did not include PAHs and was composed of polar compounds that were efficiently ionized by ESI. The first-stage POA had an average O/C of 0.65 and 0.56 for *n*-pentane and *n*-heptane, respectively, and thus falls under OOA, a category previously reserved for SOA (*4*, *28*, *29*). Furthermore, ESI-MS spectra show repetitive clusters of peaks separated by 14 u, which is indicative of oligomer formation (*30*), another feature usually associated with SOA (*31*–*33*) and is further explored in the subsequent section. It is possible that the first-stage POA included some reduced species that were not detected by ESI-MS, but the fact that it was completely transparent to LDI-MS indicates that reduced species, if any, did not constitute a substantial fraction.

These results demonstrate a marked difference in chemical characteristics between first-stage POA and traditional hydrocarbon combustion POA (i.e., second-stage POA), which necessitates distinction between the two. To facilitate use within the context of atmospheric chemistry, we introduce the term OxyPOA to refer to first-stage POA. OxyPOA communicates the most distinct aspect of first-stage POA, namely, high O/C, and maintains the same general terminological character used to describe OA in atmospheric chemistry literature (POA, SOA, HOA, OOA, etc.). We note that OxyPOA is different from oxidized POA, a term used to refer to aged POA that has undergone heterogeneous oxidation in the atmosphere (*34*, *35*). We also note that although first-stage POA, or OxyPOA, is essentially organic particulate combustion emissions, it does not form through the high-temperature soot-formation route (*36*) and therefore should not be subsumed under the term 'incipient soot' (*14*). The formation pathways of OxyPOA, described in the subsequent section, differ from those of furans, which involve incorporation of oxygen into PAH structures in the high-temperature region of hydrocarbon flames (*37*). Furthermore, furans and other oxygenated species that form at high temperatures in flames usually have relatively small O/C (*37*), consistent with HOA (traditional hydrocarbon combustion POA).

Formation pathways of OxyPOA

Collisionally stabilized alkylperoxy radicals (RO_2) traverse unimolecular reactions on potential energy surfaces that include

isomerization to carbon-centered QOOH radicals and concerted elimination of HO_2. The former type of reaction is central to chain branching and can also produce cyclic ether species, as in Fig. 2, in which 2-pentyl undergoes reaction with O_2 to ultimately form 2-methyltetrahydrofuran, which is one of several isomers formed during *n*-pentane oxidation (*38*). Similar to alkyl radicals, cyclic ethers also undergo complex reactions with O_2 (*39*–*41*). In addition to unimolecular reactions, however, RO_2 radicals can undergo bimolecular reactions including with other RO_2 radicals (*42*). Figure 2 depicts, as an example, a set of reactions of 2-methyltetrahydrofuran that produce highly oxidized, multifunctional intermediates in sequential steps mediated by organic hydroperoxides (ROOH), which result in species of decreased volatility that can partition to the particle phase and contribute to OxyPOA formation.

2-Methyltetrahydrofuran ($C_5H_{10}O$) and 2-methyltetrahydrofuran-3-one ($C_5H_8O_2$) were detected in the gas-phase emissions of first-stage *n*-pentane combustion. Both species had temperature-dependent concentration profiles that exhibited similar trends to that of OxyPOA (fig. S4), signifying their role as OxyPOA precursors. As illustrated in Fig. 2, 2-methyltetrahydrofuran-3-one can undergo two additional oxygen addition steps leading to the formation of $C_5H_6O_3$ molecules [2-methylfuran-3,4(2*H*,5*H*)-dione and 3-oxotetrahydrofuran-2-carbaldehyde] and ultimately $C_5H_4O_4$ molecules [5-methylfuran-2,3,4(5*H*)-trione and 3,4-dioxotetrahydrofuran-2-carbaldehyde]. The intermediate $C_5H_6O_3$ molecules were not detected in the gas phase, which is ascribed to their existence at concentrations below the detection limit of our gas-phase instruments. Furthermore, their volatility is appreciably high, such that partitioning to the particle phase is precluded (fig. S5). The $C_5H_4O_4$ molecules, however, have volatilities low enough to partition to the particle phase. The *n*-pentane OxyPOA species detected by ESI-MS included a peak at mass/charge ratio (*m*/*z*) 128.011 that reflects a molecular formula $C_5H_4O_4$, which coincides with 5-methylfuran-2,3,4(5*H*)-trione and 3,4-dioxotetrahydrofuran-2-carbaldehyde in Fig. 2.

Other pathways to multifunctional species include the formation of dicarbonyls via oxidation of the tertiary radical of *syn*-2,4-dimethyloxetane, another cyclic ether derived from *n*-pentane (*41*). Figure S7 illustrates the formation of 2,4-pentanedione ($C_5H_8O_2$) (detected in the gas phase of first-stage *n*-pentane combustion), which undergoes further oxidation to form 2,3,4-trioxopentanal and 2,4-dioxopentanedial. Both species have molecular formula $C_5H_4O_4$, which coincides with the *m*/*z* 128.011 peak detected in the particle phase.

Note that the chemical composition of OxyPOA shares some similarity with highly oxygenated organic molecules (HOMs) (*43*) by containing multiple oxygen atoms in a hydrocarbon structure. However, the two are differentiated by the formation mechanisms: OxyPOA arises from QOOH-mediated, cyclic-ether derived reaction pathways during LTC, whereas HOMs form via autoxidation

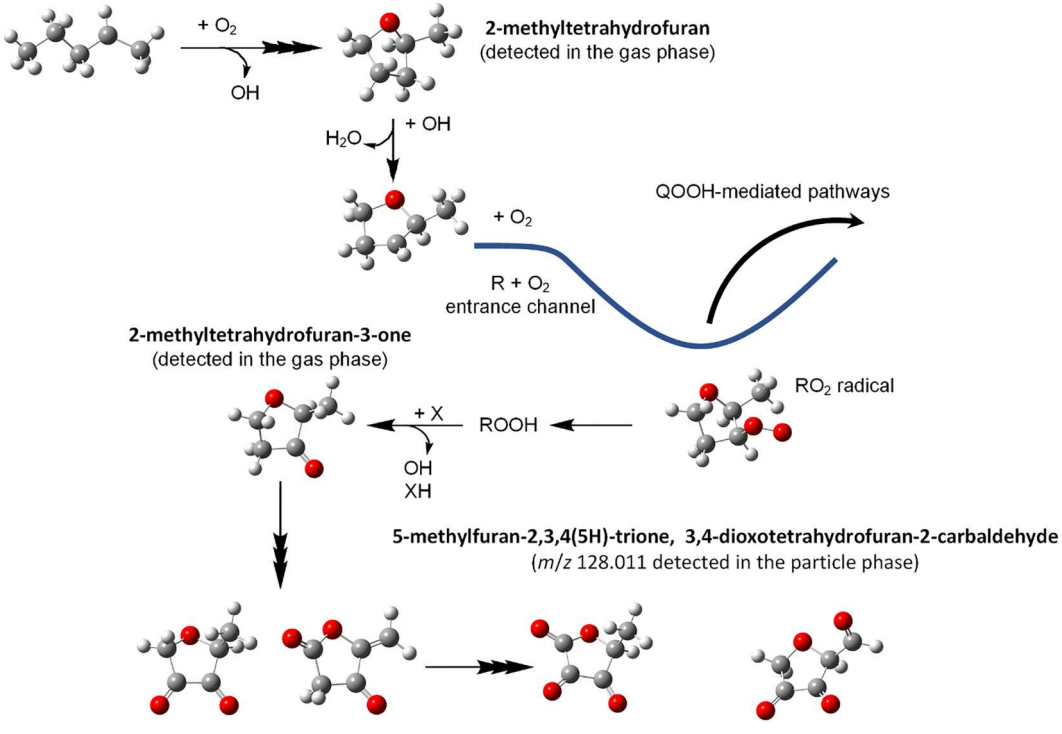

Fig. 2. Pathway for OxyPOA formation from gas-phase precursors produced during first-stage combustion of *n*-pentane. Oxidation of 2-pentyl produces 2-methyltetrahydrofuran, a cyclic ether, via a QOOH-mediated reaction. Subsequent H-abstraction and O_2-addition produces cyclic ether peroxy radicals (RO_2), such as 2-methyl-tetrahydrofuranyl-3-peroxy, which can undergo additional QOOH-mediated reactions or act as a hydrogen abstractor to produce ROOH. Abstraction of tertiary hydrogen from ROOH and barrierless O—O scission of the resultant carbon-centered radical, carbonyl-substituted species are produced coincident with OH in a chain-propagating step (*42*). Subsequent oxidation of species such as 2-methyl-tetrahydrofuran-3-one yields condensable species that form OxyPOA. The RO_2 well-depth, shown arbitrarily submerged, is typically 35 kcal/mol exothermic relative to the R + O_2 entrance channel. X denotes a generic radical, and XH denotes a closed-shell hydrogen donor. Figure S6 provides a detailed reaction scheme for other pathways involving RO_2 radicals that occur during LTC.

involving RO_2 radicals in the atmosphere and are contributors to SOA (*43*).

Supported by species detected in the gas phase and particle phase of the *n*-pentane first-stage combustion emissions, the schemes in Fig. 2 and fig. S7 provide viable pathways for OxyPOA formation from gas-phase precursors. However, this alone cannot explain the large molecular sizes observed in the mass spectra of OxyPOA species (Fig. 1 and fig. S3). Limited by the scarcity of small hydrocarbon radicals at LTC conditions, such as vinyl and propargyl, it is unlikely for gas-phase reactions to produce species with carbon numbers larger than that of the parent hydrocarbon. We hypothesize that the critical final step in OxyPOA formation is molecular growth by oligomerization. Formation of oligomers not only renders the molecules in the particle phase less volatile but also provides a condensation sink for more monomers to condense and oligomerize, thus creating a feedback mechanism that promotes condensational particle growth. We provide two levels of evidence for the prevalence of oligomers in OxyPOA: (i) patterns in the ESI-MS spectra and (ii) response to perturbation in gas-particle equilibrium partitioning.

Mass spectra of oligomers previously observed in SOA are characterized by broad groupings, with each grouping composed of clusters of equidistant peaks (*32*). Because of the high diversity of monomer combinations, the broad groupings are not apparent in the OxyPOA ESI-MS spectra (Fig. 1) but can be observed by isolating monomers with a certain carbon number. Representative results are shown in Fig. 3 for C_5 (*n*-pentane) and C_7 (*n*-heptane) monomers and oligomers with carbon numbers that are multiples of 5 and 7, respectively. These monomers form via first-stage functionalization pathways over which the hydrocarbon backbone remains intact during oxidation, resulting in C_5 (for *n*-pentane combustion) and C_7 (for *n*-heptane combustion) molecules with diverse functionality, including carbonyls and cyclic ethers, which are common products of alkane oxidation (*44*, *45*). Isolating molecules with carbon numbers C_{5c} and C_{7c} (c = 1, 2, 3, 4) in the ESI-MS spectra of the *n*-pentane OxyPOA (Fig. 3A) and *n*-heptane OxyPOA (Fig. 3C) reveals oligomer signatures similar to those previously reported for SOA (*32*). Oligomer formation is further evidenced by the relatively small change in H/C and O/C with increasing carbon number, which is consistent with growth by monomer association. One exception is noted for the O/C of the C_5 monomers in *n*-pentane OxyPOA being substantially larger than the oligomers. This can be explained as follows: Because of the small carbon number, only the highly functionalized C_5 monomers with high O/C have volatilities low enough (*46*) to partition to the particle phase, resulting in the O/C of the C_5 monomers in the OxyPOA sample being skewed high.

The broad groupings of C_{5c} and C_{7c} oligomers exhibit sequences of smaller clusters separated by 14 u. This suggests dominant formation pathways of monomers that include sequential steps with the net result of abstracting two hydrogen atoms and adding one oxygen atom (Fig. 2). Various combinations of these C_5 and C_7 monomers lead to the formation of oligomers with general formulae $C_{5c}H_{m-2i}O_{n+i}$ and $C_{7c}H_{m-2i}O_{n+i}$ (i = 1, 2, 3,...). This is illustrated in Fig. 3B and Fig. 3D, which show that all the dimers and tetramers belong to, respectively, $C_{5c}H_{m-2i}O_{n+i}$ and $C_{7c}H_{m-2i}O_{n+i}$ families (c = 2, 4). The various combinations of monomers (with varying carbon numbers) that form through similar hydrogen abstraction and oxygen addition pathways manifest as tightly packed oligomer structures separated by 14 u (Fig. 1).

To further confirm the role of oligomerization in OxyPOA formation, we examined the response of *n*-pentane OxyPOA to either dilution with clean air or heating in a thermodenuder. In the absence of oligomers, the extent of evaporation in response to both perturbations would be dictated by internally consistent thermodynamic properties (volatility distribution) of the aerosol components. The presence of oligomers, however, leads to an evaporation response that is limited by the rate of oligomer dissociation, which increases substantially with increasing temperature (*47*). This would manifest as an apparent thermodynamic inconsistency in the aerosol response to the two perturbations: The aerosol would appear more volatile in the thermodenuder perturbation compared to dilution.

The dilution perturbation led to minimal evaporation (Fig. 4C), in agreement with equilibrium partitioning calculations using volatility distribution estimated from ESI-MS molecular assignments. This indicates that the estimated volatility distribution, while not meant to be exact, predicted reasonably well the fraction of species that measurably partitioned to the gas phase in response to dilution (intermediate-volatility and semi-volatile compounds). However, equilibrium partitioning calculations using the same volatility distribution severely underestimated the extent of evaporation in the thermodenuder (Fig. 4A). Reproducing the OxyPOA response to the thermodenuder perturbation required substantially shifting the volatility distribution toward higher-volatility components, which would overestimate the extent of evaporation in response to dilution. As we argue above, this seeming thermodynamic inconsistency signifies a prominent role of oligomer dissociation (*47*).

Prevalence of OxyPOA in engine emissions

We performed LDI-MS and ESI-MS analysis on POA samples collected from the emissions of a spark-ignition (gasoline) engine operated at a simulated cold-start condition and a compression-ignition (diesel) engine operated at steady-state conditions using either conventional diesel combustion (CDC) strategy or an ACI strategy [premixed charge compression ignition (PCCI)]. As shown in Fig. 1, the cold-start POA was transparent to LDI-MS but was detected by ESI-MS and exhibited repetitive peaks separated by 14 u with an average O/C within the OOA range. These results indicate that the POA from the simulated cold-start emissions was dominated by OxyPOA. Most of the POA emissions from on-road gasoline vehicles occur during cold-start conditions (*48*), which are especially important in urban settings where a large share of driving consists of short trips at cold engine conditions (*49*). Therefore, we expect OxyPOA to be ubiquitous in urban atmospheres.

Both CDC and PCCI emitted POA with typical soot-formation signatures identified by LDI-MS, signifying the presence of second-stage POA (Fig. 1). ESI-MS detected species in the PCCI POA but not the CDC POA. Similar to the cold-start POA, the PCCI POA species measured by ESI-MS had O/C within the OOA range and the spectra exhibited repetitive peaks, albeit not as prominent as the cold-start POA, possibly due to the lower signal. These results suggest that the lower global in-cylinder temperatures in PCCI compared to CDC (*50*) resulted in a portion of the emissions experiencing temperature histories (550 to 750 K) conducive to the formation of first-stage POA (OxyPOA). Previous studies have reported

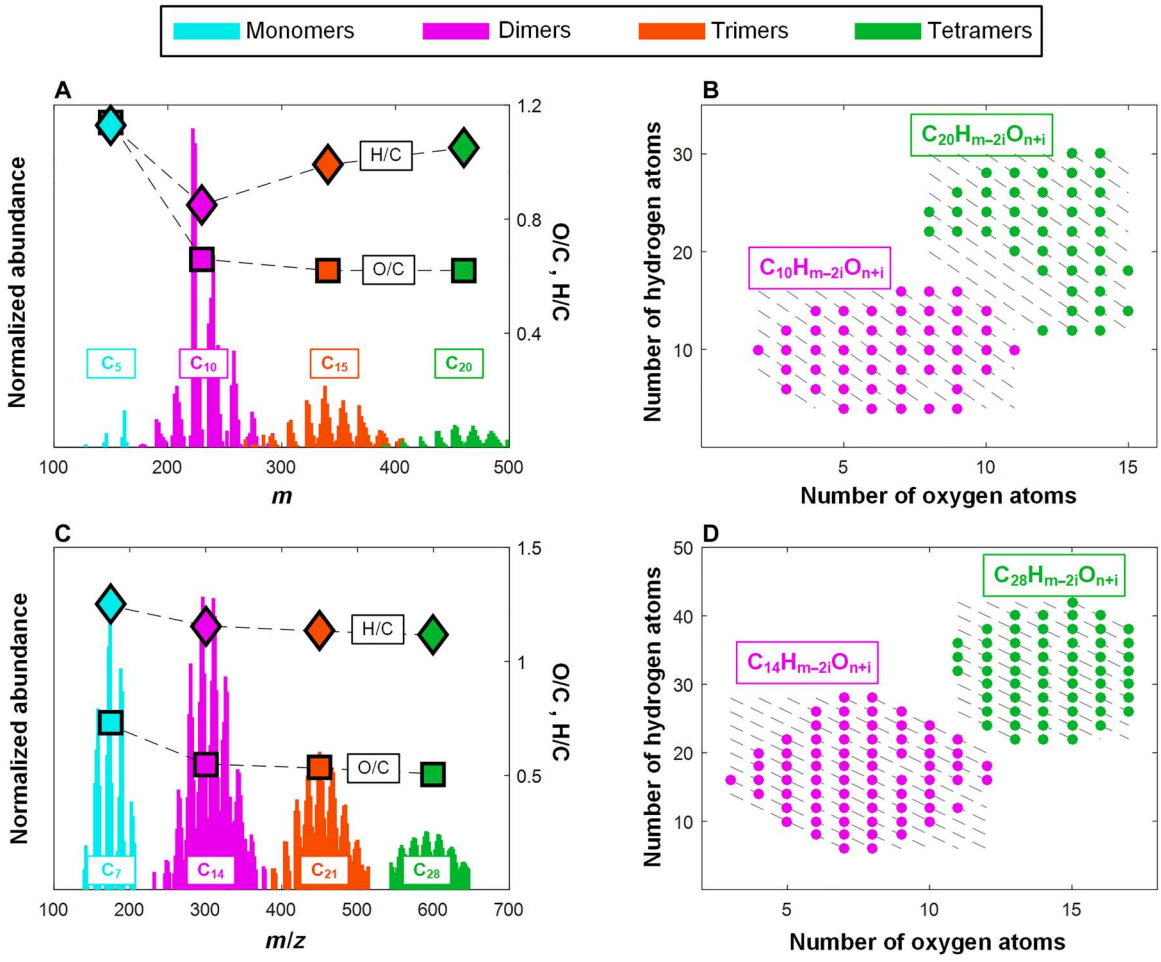

Fig. 3. Evidence for oligomer formation from ESI-MS analysis. (**A** and **C**) ESI-MS spectra of OxyPOA in *n*-pentane and *n*-heptane combustion that isolate C_5 monomers (*n*-pentane, A) and C_7 monomers (*n*-heptane, C) and oligomers with carbon numbers that are multiples of 5 and 7, respectively. Also shown are the average H/C and O/C of the monomers and the oligomers. (**B** and **D**) Number of hydrogen atoms versus number of oxygen atoms of the dimers and tetramers. (B) All the dimers and tetramers in the *n*-pentane OxyPOA belong to families with the general formula $C_{10}H_{m-2i}O_{n+i}$ and $C_{20}H_{m-2i}O_{n+i}$ (dashed gray lines), respectively. (D) All the dimers and tetramers in the *n*-heptane OxyPOA belong to families with the general formula $C_{14}H_{m-2i}O_{n+i}$ and $C_{28}H_{m-2i}O_{n+i}$ (dashed gray lines), respectively. Results consistent with those in (C) and (D) for *n*-heptane were obtained using nano-DESI MS (fig. S3).

substantial increase in emissions of POA relative to mature soot for various ACI strategies (*51*, *52*). Our results indicate that a fraction of this POA is OxyPOA.

DISCUSSION

The discovery of OxyPOA reported in this study can help solve a long-standing mystery associated with air-quality models persistently predicting lower SOA levels in urban regions compared to observations (*53*–*56*). SOA formation in air quality models is simulated on the basis of parameterizations derived from smog-chamber experiments that involve oxidizing SOA precursors found in the emissions of various sources, including vehicle emissions. Several culprits have been proposed as possible explanations for the underestimation of SOA formation in these parameterizations, including missing precursors (*53*) and underestimation of SOA yields of precursors in vehicle emissions (*57*). Intermediate-volatility organic compounds (IVOCs) and semi-volatile organic compounds (SVOCs) in vehicle emissions, which have particularly high SOA yields, have been hypothesized to be among the missing SOA precursors (*58*). However, a recent modeling study concluded that accounting for IVOCs and SVOCs played a minor role in closing the gap between modeled and measured SOA over urban areas in southern California (*56*). Another proposed explanation is vapor wall loss artifacts in smog chamber experiments leading to underestimation of SOA yields in the derived parameterizations (*55*, *56*). We provide an alternative explanation: The gap between modeled and measured SOA in urban atmospheres is partly due to overestimation of SOA in atmospheric observations, rather than underestimation in models. Atmospheric measurements equate POA from vehicle emissions to HOA and SOA to OOA. However, our results suggest that OxyPOA constitutes a substantial fraction of urban POA emitted from gasoline vehicles during cold-start. Consequently, OxyPOA would be counted as OOA and misattributed to SOA in atmospheric measurements, leading to overestimation of SOA.

Quantifying the levels of OxyPOA in urban atmospheres, however, requires further investigation. On the atmospheric

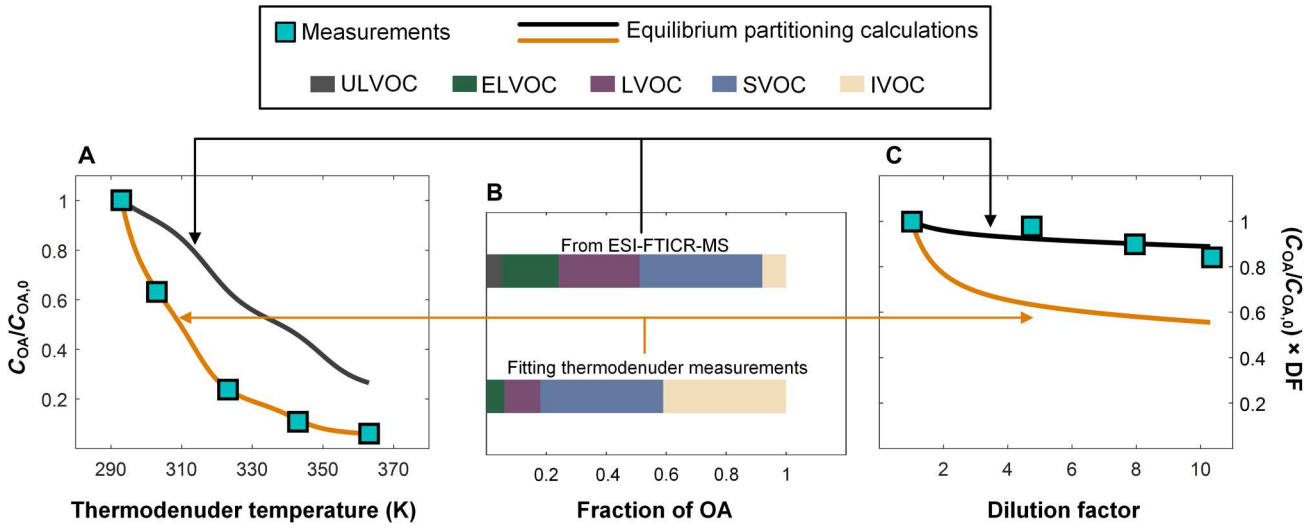

Fig. 4. Evidence for presence of oligomers in OxyPOA from comparing evaporation measurements of *n*-pentane OxyPOA to equilibrium partitioning calculations. (**A**) Thermodenuder measurements showing the aerosol mass concentration at each temperature (C_{OA}) relative to the aerosol mass concentration at the reference temperature ($C_{OA,0}$). Also shown are equilibrium partitioning calculations using volatility distribution obtained from ESI-MS molecular assignments (black line). The brown line corresponds to equilibrium partitioning calculations using a volatility distribution adjusted to reproduce the measurements. (**B**) Volatility distributions obtained from ESI-MS molecular assignments (top bar) and adjusted to reproduce the thermodenuder measurements (bottom bar). The aerosol components are apportioned into intermediate-volatility (IVOC), semi-volatile (SVOC), low-volatility (LVOC), extremely low-volatility (ELVOC), and ultralow-volatility (ULVOC) organic compounds. (**C**) Dilution measurements showing C_{OA} at a certain dilution factor (DF) relative to no dilution ($C_{OA,0}$). Dilution leads to a decrease in C_{OA} because of dilution itself and evaporation. To isolate the effect of evaporation, the *y* axis is scaled by DF, such that the case of no evaporation would show as a horizontal line with a value of 1. Also shown are equilibrium partitioning calculations using volatility distribution obtained from ESI-MS molecular assignments (black line) and volatility distribution adjusted to reproduce the thermodenuder measurements (brown line).

measurements front, this entails identifying molecular markers and/or factors that distinguish OxyPOA from anthropogenic SOA. Representing OxyPOA in air-quality models requires incorporating it as a separate POA category alongside traditional POA in vehicle emission inventories. This, in turn, requires performing measurements to quantify emission factors of OxyPOA that take into account variables such as emission certification standards, driving conditions, fuel blends, among others.

The detection of OxyPOA in the emissions of the PCCI engine (Fig. 1) suggests a relative increase in OOA compared to HOA in future urban atmospheres if these next-generation ACI strategies are widely adopted. Quantifying OxyPOA in ACI engine emissions is critical for obtaining a comprehensive understanding of their emission profiles to devise control strategies that aid in the development of clean, sustainable transportation energy technologies (*59*).

MATERIALS AND METHODS

n-Pentane and *n*-heptane controlled combustion experiments

The setup used to generate first-stage and second-stage POA from the controlled combustion of *n*-pentane and *n*-heptane is shown in fig. S8 and is described in detail in previous studies (*13*, *16*, *60*, *61*, *62*). Briefly, fuel oxidation was temperature-initiated in a 0.24-liter custom-built cylindrical quartz chamber enclosed in an insulated heater (Thermcraft Inc., NC, USA). Temperature was controlled to within 1 K using a proportional-integral-derivative (PID) controller (OMEGA, CNi3244) using a high-temperature K-type thermocouple located at the center of the chamber. Fuel was introduced via a bubbler system using a mass flow controller (DAKOTA, 6AGC1AL55-09AB) to direct a stream of ultrahigh-purity N_2 (NI UHP300, Airgas) into a bubbler containing the fuel. The bubbler dimensions were designed to ensure that the N_2 stream was fully saturated with the fuel vapor at the exit of the bubbler, as verified by mass transfer calculations confirming that the residence time of a bubble rising in the bubbler is greater than the time required to saturate it with the fuel vapor (*61*). This allowed us to calculate the flowrate of the fuel entering the combustion chamber based on the fuel saturation pressure and N_2 flowrate. The fuel-saturated N_2 stream was then mixed with a controlled stream of clean dry air and N_2 to maintain an equivalence ratio (ϕ) of 2.3 and O_2/N_2 of 0.06.

The total flowrate into the combustion chamber was 0.75 standard liters per minute (SLPM), resulting in average residence time of approximately 19 s. The combustion emissions were then diluted in a 4-liter glass dilution chamber with 12 SLPM of clean dry air before POA sampling. To observe first-stage and second-stage POA formation, the temperature of the combustion chamber was varied between 500 and 1300 K and the size distributions of the POA emissions were continuously monitored at 90-s time resolution using a scanning mobility particle sizer (TSI model 3088). The size distributions were integrated using a particle effective density of 1.3 g/cm^3, estimated using tandem differential mobility analyzer—aerosol particle mass analyzer (tandem DMA-APM) technique (*13*, *63*)—to obtain temperature-dependent POA mass concentration profiles. As shown in fig. S1, both *n*-pentane and *n*-heptane exhibited two-stage aerosol formation. The first-stage POA peak emission was at 583 and 563 K for *n*-pentane and *n*-heptane, respectively.

We collected POA samples on 47-mm polytetrafluoroethylene (PTFE) filters (0.2-μm pore size, Whatman) for the chemical analyses described below. The collection flowrate was 5 SLPM, and the targeted mass loading was 300 μg to avoid filter clogging, which occurs at ~350 μg. Filters were stored at −15°C pending analysis. First-stage POA samples were collected at combustion temperature of 583 and 563 K for *n*-pentane and *n*-heptane, respectively. Second-stage POA samples were collected at combustion temperature of 1123 and 1308 K for *n*-pentane and *n*-heptane, respectively.

We also collected samples from *n*-pentane combustion for gas-phase chemical analysis (described below) using a 1-gallon (3.8-liter) stainless steel double-ended sample cylinder (304 L-HDF4-1GAL, Swagelok) fitted with ¼ inch needle valves on both ends (fig. S8). The combustion emissions were sampled directly into the cylinder from the combustion chamber (without dilution) at a flowrate of 0.5 SLPM, and the valves at the inlet and outlet of the cylinder were closed once steady-state conditions were achieved. The POA was removed from the emissions using a PTFE filter before entering the cylinder. To compare the temperature-dependent concentration profiles of gas-phase species emitted during first-stage combustion to that of first-stage POA, we collected gas-phase samples at five temperature points: 543, 563, 598, 658, and 743 K. The second-stage gas-phase samples were collected at 1143 K.

Cold-start spark-ignition engine experiments

A single-cylinder version of a GM LNF 2.0L direct-injected spark-ignited four-cylinder engine was used for these experiments, wherein three of the cylinders were disabled by grinding off the cam lobes to prevent valve actuation and by drilling holes in the pistons to prevent compression. More details of the engine setup, instrumentation, and cold-start operation are available in previous studies on this engine (*64*, *65*). Briefly, the firing cylinder was maintained in stock configuration, wherein the compression ratio, combustion chamber geometry, fuel injector, cam lobe profiles, and cam phasing capabilities were all stock. The engine was fueled with a nine-component surrogate fuel blend known as PACE20 that was designed by the Partnership to Advance Combustion Engines (PACE) consortium to closely mimic the fuel properties such as boiling range and octane rating, as well as engine emissions parameters such as sooting propensity of a market-representative 87 anti-knock index E10 fuel while eliminating fuel composition uncertainties from chemical kinetics modeling. The fuel composition and properties are detailed elsewhere (*65*). Cold-start operation was simulated by operating the engine at 1300 rpm and 2-bar net indicated mean effective pressure stoichiometric operation, while the engine out coolant and oil temperature were controlled to 20°C. For this study, spark timing was used as the engine control parameter to study engine emissions under normal and cold-start conditions. For the data presented in this study, the spark timing was fixed at 25 degrees after-top-dead-center-firing and the exhaust gas was sampled 35-mm downstream of the exhaust port.

Compression-ignition engine experiments

The CDC and a PCCI samples were collected from the exhaust of a single-cylinder medium-duty diesel engine. A complete description of the engine and mode operation has been previously described (*66*). Briefly, a 6.7-liter Cummins 6-cylinder ISB engine was modified to single-cylinder operation by deactivating five cylinders and running these samples on certified ultralow-sulfur diesel no. ULSD #2 fuel. The same engine was operated in both the CDC and PCCI modes to collect filters samples of aerosol emissions. A similar dilution tunnel setup, as that described for the cold-start experiments, was used to collect aerosol samples on PTFE filters. Both samples were collected at 1200 rpm, but the PCCI samples was at low load (1.8 bar), and the CDC sample was at high load (3.2 bar) (*67*).

POA chemical analysis using LDI-MS

The POA samples shown in Fig. 1 were analyzed using LDI-MS at the University of Georgia′s Proteomics and Mass Spectrometry Core Facility. LDI-MS is efficient at detecting incipient soot and has been extensively used to study soot formation from various combustion sources (*17*, *68*, *69*). We extracted the POA filter samples by sonicating in 2 ml of dichloromethane (DCM) for 40 min. The solutions were then concentrated to 1 ml by evaporation using a gentle stream of ultrahigh-purity N_2. The solutions were then spotted onto a stainless-steel grid for LDI-MS analysis in 250-μl batches, allowing the DCM to evaporate after each batch. On the basis of our experience (*13*, *16*, *27*) and in concordance with previous studies (*23*, *69*, *70*, *71*), we chose DCM as a solvent for LDI-MS analysis due to its efficacy at extracting large molecular size PAHs that constitute incipient soot. LDI-MS analysis was performed on a Bruker Autoflex III in reflectron mode using AutoXecute. Calibration was performed using 2,5 dihydroxybenzoic acid (MH = 255.0 *m*/*z*; monoisotopic mass), reserpine (609.3 *m*/*z*; monoisotopic mass), angiotensin (MH^+ = 1296.7 *m*/*z*; monoisotopic mass), and insulin (5734.5 *m*/*z*; average mass). The instrument uses a 337 nm Nitrogen laser in positive mode. The ion source was set to 19 kV, and the reflector voltage was set to 20 kV. Random walk with the raster was set to 2 shots per spot with a total of 100 laser shots. The samples were analyzed within two molecular size ranges, 100 to 1000 *m*/*z* and 1000 to 2000 *m*/*z*. The instrument sensitivity was set just below saturating the largest signal within each range to detect the large molecular size PAHs (Fig. 1A), which would otherwise go undetected if the same sensitivity was applied for the full range (100 to 2000 *m*/*z*).

POA chemical analysis using ESI-MS

The POA samples shown in Fig. 1 were analyzed using ESI Fourier transform ion cyclotron resonance MS (ESI-FTIRC-MS) at the University of Georgia′s Proteomics and Mass Spectrometry Core Facility. ESI-MS is efficient at detecting relatively polar molecules (*72*–*74*) and has been previously used to perform chemical analysis on various types of OA samples, including biomass-burning OA (*74*–*76*), SOA (*77*–*79*), and urban OA (*80*, *81*).

For ESI-FTIRC-MS analysis, the POA filters were extracted using the same procedure described above for LDI-MS analysis but using acetonitrile as a solvent because of its efficacy at extracting polar compounds (*79*, *82*, *83*). An extraction blank with a clean PTFE filter was also prepared following the same steps and was used for background correction. Analysis was performed on a Bruker SolariX 12 T FTICR mass spectrometer (Bruker Daltonik, GmbH, Bremen, Germany) in negative ion mode. Mass spectra were collected between 75 and 1000 *m*/*z* with 2 M data point length and a 0.4194-s transient. Time of flight was set at 0.8 ms. Samples were infused at a rate of 2.0 μl/min. The capillary voltage was set to 4500 V with a −800 V end plate offset. The nebulizer gas was set to 0.5 bar, and the dry gas was set to 4.0 liter/min with a dry

temperature of 200°C. Ion accumulation time was 0.005 s. Calibration was performed with sodium trifluoroacetate (Sigma-Aldrich) (0.1 mg/ml in 50:50 methanol:water). Spectra were collected in triplicate by doing three injections of 10 μl of sample. Before introducing samples to the instrument, methanol and extraction blanks were acquired.

For data analysis, 48 scans per injection per sample were averaged using Bruker Compass Data Analysis software (version 5.3). Background subtraction was performed using Xpose mode with a retention time window of 0.0083 s and a ratio of 5 to minimize noise signals and signals that were detected in the extraction blanks. MFAssignR (*84*), an open source R package, was used to analyze the data according to component molecular formulae. Assignments were internally recalibrated and subjected to the following restrictions: $C_xH_yO_z$, $0.3 \leq H/C \leq 3$, $0 \leq O/C \leq 2.5$, and a maximum allowable error of ≤1 parts per million (ppm). The final peak list that represents each sample is composed of molecular formulae that are common across the three injections. The number of molecular assignments was 1014 for *n*-pentane first-stage POA, 1525 for *n*-heptane first-stage POA, 206 for the cold-start spark-ignition engine POA, and 185 for the PCCI engine POA. The *n*-pentane second-stage POA, *n*-heptane second-stage POA, and CDC POA had no signal. Average O/C values shown in Fig. 1C were calculated as signal-weighted averages of O/C values of the individual molecules identified in the ESI-MS spectra.

POA chemical analysis using nanospray desorption ESI-MS

In addition to ESI-FTIRC-MS, the *n*-heptane first-stage POA was also analyzed at the Pacific Northwest National Laboratory Environmental Molecular Sciences Laboratory using nanospray desorption ESI (nano-DESI) high-resolution MS (HRMS). The design of the nano-DESI HRMS interface has been previously described in (*85*, *86*). Briefly, a 7:3 (v/v) acetonitrile/water solvent mixture (Optima LC-MS grade, Fisher Chemical, Hampton USA) was flowed at 0.5 μl/min through a capillary assembly formed by two fused silica capillaries aligned at ~90° [Polymicro Technologies, Phoenix, USA; primary capillary: 150 μm in outer diameter (O.D.), 50 μm in inner diameter (I.D.); secondary capillary: 150-μm O.D., 20-μm I.D. with etched terminus (*87*)]. This junction was brought sufficiently close to the PTFE filter samples, such that a liquid junction formed and scanned along the *XY* plane at 35 μm/s, allowing for continuous and direct sampling from the filters. A −3.5 kV was applied via the solvent syringe needle, and the nano-DESI capillary assembly was positioned ~1 mm from the inlet of a high-resolution LTQ Velos Orbitrap mass spectrometer (Thermo Fisher Scientific, Waltham). The MS inlet was maintained at 275° C. All samples were analyzed in negative ion mode via MS1 (m/z 100 to 1000) with an automatic gain control target of 5 × 105, maximum ion injection time of 500 ms, and mass resolution of 100,000 at m/z 400.

For data analysis, 100 scans were averaged per sample within Xcalibur (Thermo Fisher Scientific) and exported as a .csv peak list (5 decimal points per m/z). MFAssignR was used for component molecular formulae assignment. For features with S/N > 6, assignments were internally recalibrated and subjected to the following restrictions: $C_xH_yO_z$; $0.3 \leq H/C \leq 3$; $O/C \leq 2.5$; $-20 \leq DBE\text{-}O \leq 25$ [double bond equivalents minus oxygen count (DBE-O)]. Datasets were blank subtracted, such that molecular formulae detected in both a solvent blank and sample list were removed from the final sample list if they were present in the sample at 3× or lower the level found in the blank. Final datasets were manually inspected/cleaned for outlier assignments (*86*). The final peak list used in the interpretations for each sample is composed of only molecular formulae commonly detected across each of three replicates. The number of molecular assignments was 1895 for *n*-heptane first-stage POA.

Gas-phase chemical analysis using electron-impact MS and vacuum ultraviolet absorption spectroscopy

Using a filtration system to remove particles, gas-phase samples were collected for offline analysis from the controlled combustion of *n*-pentane. To compare the temperature-dependent concentration profiles of gas-phase species emitted during first-stage combustion to that of first-stage POA, we collected gas-phase samples at five temperature points: 543, 563, 598, 658, and 743 K. The second-stage samples were collected at 1143 K. Gas-phase samples were compressed in an inert-coated chamber and then introduced into a valving system connected to a gas chromatograph (GC), which collects 500 μl of the sample. The 500-μl volume was then introduced via the GC to three different detectors. First, the sample was directed through a 5-Å molecular sieve—which separates CO, CO_2, H_2, O_2, and CH_4,—for analysis via a thermal conductivity detector using Ar as reference gas. The filtered sample was then split into two volumes of 250 μl, which are injected sequentially onto two identical paraffins, olefins, naphthene and aromatics (PONA) columns of 100 m in length, 250 μm in I.D., and 0.50 μm in film thickness. The two columns follow the same temperature programming, which begins with holding at 40°C for 5 min, increasing to 110°C at 5° C/min, holding at 110°C for 5 min, increasing to 280°C at 5°C/min, and holding at 280°C for 5 min.

One PONA column leads to a 70-eV electron-impact mass spectrometer, while the other leads to a vacuum-ultraviolet (VUV) absorption cell, which is held at 50°C and 795 ± 2 torr. Species quantification was achieved through fitting of measured absorption spectra to reference spectra at photon energies with high signal-to-noise ratios lying within the full-scale range of 5.17 to 9.92 eV. Before quantification, reference spectra were created from injection of reference gas samples, typically at 1000 ppm. VUV spectra of the detected species are shown in figs. S9 to S17.

Gas-particle partitioning perturbation experiments

To assess the effect of oligomer dissociation on the evaporation behavior of OxyPOA, we subjected the OxyPOA emissions from *n*-pentane combustion to two perturbations: (i) dilution with clean air at room temperature and (ii) heating in a thermodenuder at temperatures ranging between 303 and 363 K. Both dilution and heating perturb the gas-particle equilibrium partitioning and force the particles to evaporate to reestablish equilibrium. If the particle phase contains oligomers, then the perturbation induces not only physical evaporation (i.e., partitioning of molecules from the particle phase to the gas phase) but also oligomer dissociation (*47*). The reason is that monomers evaporate more readily than the oligomers due to their smaller molecular size, thus higher volatility. This perturbs the monomer-oligomer equilibrium in the particle phase, leading to oligomer dissociation to reestablish equilibrium. Quantifying the equilibrium composition of monomers and oligomers is not straightforward. However, the dissociation rate constant is known to increase substantially more than the association rate constant with increase in temperature (*47*). In other words, the monomer-

oligomer equilibrium composition shifts toward higher fraction of monomers as temperature increases, making the aerosol more volatile because monomers are more volatile than oligomers. Consequently, the effect of oligomer dissociation would be more prominent if the aerosol is heated in a thermodenuder compared to dilution at room temperature. Here, we probe this temperature-dependent oligomer dissociation effect by comparing the apparent volatility of the OxyPOA, namely, saturation concentration (C_{sat}), needed to explain the extent of evaporation in the dilution versus thermodenuder perturbations. If higher C_{sat} values are required to reproduce the observed evaporation in the thermodenuder measurements compared to dilution, then this would be evidence that the OxyPOA contains oligomers.

In both the dilution and thermodenuder experiments, the combustion chamber temperature was set to 583 K, corresponding to the peak OxyPOA emissions (fig. S1). The thermodenuder experiments involved in diluting the combustion emissions (0.75 SLPM) with 12 SLPM of clean air and then alternating between measuring the baseline aerosol mass concentration at room temperature ($C_{OA,0}$) by sampling through the bypass and measuring the aerosol mass concentration (C_{OA}) at 303, 323, 343, and 363 K by sampling through the thermodenuder (fig. S8). The thermodenuder consisted of a stainless-steel tube wrapped with heating tape and insulation. The temperature was controlled using a PID controller (OMEGA, CNi3244). The thermodenuder has a volume of 0.5 liters (diameter = 2.54 cm, length = 1 m), and the aerosol flow was 1 SLPM, yielding an average residence time of 30 s. In the dilution experiments, we first obtained a baseline aerosol mass concentration ($C_{OA,0}$) by mixing the combustion emissions (0.75 SLPM) with 3 SLPM of clean air in the dilution chamber (fig. S8). We then applied three dilution factors (DFs) of approximately 5, 8, and 10, and measured the aerosol mass concentration (C_{OA}) at each DF. The aerosol emissions in the dilution experiment were also sampled through the thermodenuder, but without heating, to allow for ample time for evaporation.

We performed gas-particle equilibrium calculations (*88*) to interpret the observed OxyPOA evaporation at the dilution and thermodenuder experimental conditions. We first calculated the reference saturation concentration at 300 K ($C_{sat,ref}$) of the each of the assigned molecules (see above for molecular assignments) based on the parameterization of Li *et al.* (*89*):

$$\log_{10}(C_{sat,ref}) = (n_C^0 - n_C)\ b_C - n_O\ b_O - 2\ \frac{n_C\ n_O}{n_C + n_O}\ b_{CO} \quad (1)$$

where, n_C is the number of carbon atoms, n_O is the number of oxygen atoms, $n_C^0 = 22.6$, b_C = 0.4481, b_O = 1.656, and b_{CO} = − 0.779.

The molecules were then grouped into five volatility bins that correspond to:

1) IVOCs: $C_{sat,ref} > 300\ \mu g/m^3$.

2) SVOCs: $0.3\ \mu g/m^3 < C_{sat,ref} < 300\ \mu g/m^3$.

3) Low-volatility organic compounds (LVOCs): $3 \times 10^{-4}\ \mu g/m^3 < C_{sat,ref} < 0.3\ \mu g/m^3$.

4) Extremely LVOCs (ELVOCs): $3 \times 10^{-9}\ \mu g/m^3 < C_{sat,ref} < 3 \times 10^{-4}\ \mu g/m^3$.

5) Ultra LVOCs (ULVOCs): $C_{sat,ref} < 3 \times 10^{-9}\ \mu g/m^3$.

We then assigned $C_{sat,ref}$ value for each bin, calculated as the average $C_{sat,ref}$ of the components in the bin. We calculated C_{sat} values at different temperatures [$C_{sat}(T)$] using the Clausius-Clapeyron relation

$$C_{sat}(T) = C_{sat,ref}\ \frac{T_{ref}}{T}\ \exp\left[\frac{-\Delta H}{R}\ \left(\frac{1}{T} - \frac{1}{T_{ref}}\right)\right] \quad (2)$$

where T_{ref} is the reference temperature (300 K), R is the universal gas constant, and ΔH is the enthalpy of vaporization, estimated using the parameterization of Epstein *et al.* (*90*)

$$\Delta H\ [\mathrm{kJ/mol}] = -11 \log_{10}(C_{sat,ref}) + 129 \quad (3)$$

We then used an iterative solution to calculate C_{OA} at each experimental condition (for both dilution and thermodenuder experiments) following Donahue *et al.* (*88*)

$$z_i = \left(1 + \frac{C_{sat,i}}{C_{OA}}\right)^{-1};\ C_{OA} = \sum_i C_i\ z_i \quad (4)$$

where, the subscript "i" refers to a specific volatility bin, z is the portioning coefficient between the particle phase and the gas phase, and C is the total concentration in both phases.

The equilibrium-partitioning C_{OA} values calculated using the volatility distribution obtained from molecular assignments correspond to the black lines in Fig. 4 (A and C). We also obtained a volatility distribution that yields equilibrium-partitioning C_{OA} values that fit the thermodenuder measurements by adjusting the mass fractions in the volatility bins. These equilibrium-partitioning C_{OA} values correspond to the brown lines in Fig. 4 (A and C).

Supplementary Materials

This PDF file includes:

Supplementary Text
Figs. S1 to S17
References

REFERENCES AND NOTES

1. D. W. Dockery, C. A. Pope, X. Xu, J. D. Spengler, J. H. Ware, M. E. Fay, B. G. Ferris Jr., F. E. Speizer, An association between air pollution and mortality in six U.S. cities. *N. Engl. J. Med.* **329**, 1753–1759 (1993).
2. T. Pervin, U.-G. Gerdtham, C. H. Lyttkens, Societal costs of air pollution-related health hazards: A review of methods and results. *Cost Eff. Resour. Alloc.* **6**, 19 (2008).
3. D. C. R. H.-O. Pörtner, M. Tignor, E.S. Poloczanska, K. Mintenbeck, A. Alegría, M. Craig, S. Langsdorf, S. Löschke, V. Möller, A. Okem, B. Rama, "*Climate Change 2022: Impacts, Adaptation, and Vulnerability. Contribution of Working Group II to the Sixth Assessment Report of the Intergovernmental Panel on Climate Change*" (IPCC, 2022).
4. J. L. Jimenez, M. R. Canagaratna, N. M. Donahue, A. S. H. Prevot, Q. Zhang, J. H. Kroll, P. F. DeCarlo, J. D. Allan, H. Coe, N. L. Ng, A. C. Aiken, K. S. Docherty, I. M. Ulbrich, A. P. Grieshop, A. L. Robinson, J. Duplissy, J. D. Smith, K. R. Wilson, V. A. Lanz, C. Hueglin, Y. L. Sun, J. Tian, A. Laaksonen, T. Raatikainen, J. Rautiainen, P. Vaattovaara, M. Ehn, M. Kulmala, J. M. Tomlinson, D. R. Collins, M. J. Cubison, E. J. Dunlea, J. A. Huffman, T. B. Onasch, M. R. Alfarra, P. I. Williams, K. Bower, Y. Kondo, J. Schneider, F. Drewnick, S. Borrmann, S. Weimer, K. Demerjian, D. Salcedo, L. Cottrell, R. Griffin, A. Takami, T. Miyoshi, S. Hatakeyama, A. Shimono, J. Y. Sun, Y. M. Zhang, K. Dzepina, J. R. Kimmel, D. Sueper, J. T. Jayne, S. C. Herndon, A. M. Trimborn, L. R. Williams, E. C. Wood, A. M. Middlebrook, C. E. Kolb, U. Baltensperger, D. R. Worsnop, Evolution of organic aerosols in the atmosphere. *Science* **326**, 1525–1529 (2009).
5. K. Johansson, M. Head-Gordon, P. Schrader, K. Wilson, H. Michelsen, Resonance-stabilized hydrocarbon-radical chain reactions may explain soot inception and growth. *Science* **361**, 997–1000 (2018).
6. O. Welz, J. D. Savee, D. L. Osborn, S. S. Vasu, C. J. Percival, D. E. Shallcross, C. A. Taatjes, Direct kinetic measurements of Criegee intermediate (CH_2OO) formed by reaction of CH_2I with O_2. *Science* **335**, 204–207 (2012).
7. C. A. Taatjes, O. Welz, A. J. Eskola, J. D. Savee, A. M. Scheer, D. E. Shallcross, B. Rotavera, E. P. Lee, J. M. Dyke, D. K. Mok, D. L. Osborn, C. J. Percival, Direct measurements of

conformer-dependent reactivity of the Criegee intermediate CH_3CHOO. *Science* **340**, 177–180 (2013).
8. Q. Zhang, J. L. Jimenez, M. Canagaratna, J. D. Allan, H. Coe, I. Ulbrich, M. Alfarra, A. Takami, A. Middlebrook, Y. Sun, Ubiquity and dominance of oxygenated species in organic aerosols in anthropogenically-influenced Northern Hemisphere midlatitudes. *Geophys. Res. Lett.* **34**, 1–6 (2007).
9. I. Ulbrich, M. Canagaratna, Q. Zhang, D. Worsnop, J. Jimenez, Interpretation of organic components from positive matrix factorization of aerosol mass spectrometric data. *Atmos. Chem. Phys. Discuss.* **9**, 2891–2918 (2009).
10. J. D. Savee, E. Papajak, B. Rotavera, H. Huang, A. J. Eskola, O. Welz, L. Sheps, C. A. Taatjes, J. Zádor, D. L. Osborn, Direct observation and kinetics of a hydroperoxyalkyl radical (QOOH). *Science* **347**, 643–646 (2015).
11. A. S. Hansen, T. Bhagde, K. B. Moore III, D. R. Moberg, A. W. Jasper, Y. Georgievskii, M. F. Vansco, S. J. Klippenstein, M. I. Lester, Watching a hydroperoxyalkyl radical (• QOOH) dissociate. *Science* **373**, 679–682 (2021).
12. B. Rotavera, C. A. Taatjes, Influence of functional groups on low-temperature combustion chemistry of biofuels. *Prog. Energy Combust. Sci* **86**, 100925 (2021).
13. O. El Hajj, K. Atwi, Z. Cheng, A. Koritzke, M. Christianson, N. Dewey, B. Rotavera, R. Saleh, Two-stage aerosol formation in low-temperature combustion. *Fuel* **304**, 121322 (2021).
14. H. Michelsen, Probing soot formation, chemical and physical evolution, and oxidation: A review of in situ diagnostic techniques and needs. *Proc. Combust. Inst.* **36**, 717–735 (2017).
15. T. C. Bond, S. J. Doherty, D. W. Fahey, P. M. Forster, T. Berntsen, B. J. DeAngelo, M. G. Flanner, S. Ghan, B. Kärcher, D. Koch, S. Kinne, Y. Kondo, P. K. Quinn, M. C. Sarofim, M. G. Schultz, M. Schulz, C. Venkataraman, H. Zhang, S. Zhang, N. Bellouin, S. K. Guttikunda, P. K. Hopke, M. Z. Jacobson, J. W. Kaiser, Z. Klimont, U. Lohmann, J. P. Schwarz, D. Shindell, T. Storelvmo, S. G. Warren, C. S. Zender, Bounding the role of black carbon in the climate system: A scientific assessment. *J. Geophys. Res. Atmos.* **118**, 5380–5552 (2013).
16. R. Saleh, Z. Cheng, K. Atwi, The brown–black continuum of light-absorbing combustion aerosols. *Environ. Sci. Technol. Lett.* **5**, 508–513 (2018).
17. A. Faccinetto, C. Focsa, P. Desgroux, M. Ziskind, Progress toward the quantitative analysis of PAHs adsorbed on soot by laser desorption/laser ionization/time-of-flight mass spectrometry. *Environ. Sci. Technol.* **49**, 10510–10520 (2015).
18. Y. Ju, Understanding cool flames and warm flames. *Proc. Combust. Inst.* **38**, 83–119 (2021).
19. H. Zhao, L. Wu, C. Patrick, Z. Zhang, Y. Rezgui, X. Yang, G. Wysocki, Y. Ju, Studies of low temperature oxidation of n-pentane with nitric oxide addition in a jet stirred reactor. *Combust. Flame* **197**, 78–87 (2018).
20. R. W. Wheeler, D. Downs, A. D. Walsh, 'Knock' in Internal Combustion Engines. *Nature* **162**, 893–894 (1948).
21. C. K. Westbrook, M. Mehl, W. J. Pitz, G. Kukkadapu, S. Wagnon, K. Zhang, Multi-fuel surrogate chemical kinetic mechanisms for real world applications. *Phys. Chem. Chem. Phys.* **20**, 10588–10606 (2018).
22. J. Zádor, C. A. Taatjes, R. X. Fernandes, Kinetics of elementary reactions in low-temperature autoignition chemistry. *Prog. Energy Combust. Sci.* **37**, 371–421 (2011).
23. A. Michela, A. Barbara, T. Antonio, C. Anna, Identification of large polycyclic aromatic hydrocarbons in carbon particulates formed in a fuel-rich premixed ethylene flame. *Carbon* **46**, 2059–2066 (2008).
24. B. Apicella, M. Millan, A. Herod, A. Carpentieri, P. Pucci, A. Ciajolo, Separation and measurement of flame-formed high molecular weight polycyclic aromatic hydrocarbons by size-exclusion chromatography and laser desorption/ionization time-of-flight mass spectrometry. *Rapid Commun Mass Spectrom.* **20**, 1104–1108 (2006).
25. J. A. Rundel, C. M. Thomas, P. E. Schrader, K. R. Wilson, K. O. Johansson, R. P. Bambha, H. A. Michelsen, Promotion of particle formation by resonance-stabilized radicals during hydrocarbon pyrolysis. *Combust. Flame* **243**, 111942 (2022).
26. J. A. Rundel, K. O. Johansson, P. E. Schrader, R. P. Bambha, K. R. Wilson, J. Zádor, G. B. Ellison, H. A. Michelsen, Production of aliphatic-linked polycyclic hydrocarbons during radical-driven particle formation from propyne and propene pyrolysis. *Combust. Flame*, 112457 (2022).
27. K. Atwi, A. Mondal, J. Pant, Z. Cheng, O. El Hajj, I. Ijeli, H. Handa, R. Saleh, Physicochemical properties and cytotoxicity of brown carbon produced under different combustion conditions. *Atmos. Environ.* **244**, 117881 (2021).
28. M. Canagaratna, J. Jimenez, J. Kroll, Q. Chen, S. Kessler, P. Massoli, L. Hildebrandt Ruiz, E. Fortner, L. Williams, K. Wilson, J. D. Surratt, N. M. Donahue, J. T. Jayne, D. R. Worsnop, Elemental ratio measurements of organic compounds using aerosol mass spectrometry: Characterization, improved calibration, and implications. *Atmos. Chem. Phys.* **15**, 253–272 (2015).
29. F. Mahrt, E. Newman, Y. Huang, M. Ammann, A. K. Bertram, Phase behavior of hydrocarbon-like primary organic aerosol and secondary organic aerosol proxies based on their elemental oxygen-to-carbon ratio. *Environ. Sci. Technol.* **55**, 12202–12214 (2021).
30. M. Kalberer, D. Paulsen, M. Sax, M. Steinbacher, J. Dommen, A. S. Prévôt, R. Fisseha, E. Weingartner, V. Frankevich, R. Zenobi, U. Baltensperger, Identification of polymers as major components of atmospheric organic aerosols. *Science* **303**, 1659–1662 (2004).
31. W. A. Hall IV, M. V. Johnston, Oligomer formation pathways in secondary organic aerosol from MS and MS/MS measurements with high mass accuracy and resolving power. *J. Am. Soc. Mass Spectrom.* **23**, 1097–1108 (2012).
32. M. P. Tolocka, M. Jang, J. M. Ginter, F. J. Cox, R. M. Kamens, M. V. Johnston, Formation of oligomers in secondary organic aerosol. *Environ. Sci. Technol.* **38**, 1428–1434 (2004).
33. H. K. Maben, P. J. Ziemann, Kinetics of oligomer-forming reactions involving the major functional groups present in atmospheric secondary organic aerosol particles. *Environ Sci Process Impacts* **25**, 214–228 (2023).
34. M. K. Shrivastava, T. E. Lane, N. M. Donahue, S. N. Pandis, A. L. Robinson, Effects of gas particle partitioning and aging of primary emissions on urban and regional organic aerosol concentrations. *J. Geophys. Res. Atmos.* **113**, D18301 (2008).
35. S. H. Budisulistiorini, J. Chen, M. Itoh, M. Kuwata, Can online aerosol mass spectrometry analysis classify secondary organic aerosol (soa) and oxidized primary organic aerosol (opoa)? A case study of laboratory and field studies of indonesian biomass burning. *ACS Earth Space Chem.* **5**, 3511–3522 (2021).
36. M. Frenklach, H. Wang, Detailed modeling of soot particle nucleation and growth, *in Symposium (International) on Combustion* (Elsevier, 1991), vol. 23, pp. 1559–1566.
37. K. O. Johansson, T. Dillstrom, M. Monti, F. El Gabaly, M. F. Campbell, P. E. Schrader, D. M. Popolan-Vaida, N. K. Richards-Henderson, K. R. Wilson, A. Violi, H. A. Michelsen, Formation and emission of large furans and oxygenated hydrocarbons from flames. *Proc. Natl. Acad. Sci. U. S. A.* **113**, 8374–8379 (2016).
38. J. Bugler, A. Rodriguez, O. Herbinet, F. Battin-Leclerc, C. Togbé, G. Dayma, P. Dagaut, H. J. Curran, An experimental and modelling study of n-pentane oxidation in two jet-stirred reactors: The importance of pressure-dependent kinetics and new reaction pathways. *Proc. Combust. Inst.* **36**, 441–448 (2017).
39. M. G. Christianson, A. C. Doner, M. M. Davis, A. L. Koritzke, J. M. Turney, H. F. Schaefer III, L. Sheps, D. L. Osborn, C. A. Taatjes, B. Rotavera, Reaction mechanisms of a cyclic ether intermediate: Ethyloxirane. *Int. J. Chem. Kinet.* **53**, 43–59 (2021).
40. A. C. Doner, M. M. Davis, A. L. Koritzke, M. G. Christianson, J. M. Turney, H. F. Schaefer III, L. Sheps, D. L. Osborn, C. A. Taatjes, B. Rotavera, Isomer-dependent reaction mechanisms of cyclic ether intermediates cis-2,3-dimethyloxirane and trans-2,3-dimethyloxirane. *Int. J. Chem. Kinet.* **53**, 127–145 (2021).
41. A. C. Doner, J. Zádor, B. Rotavera, Stereoisomer-dependent unimolecular kinetics of 2, 4-dimethyloxetanyl peroxy radicals. *Faraday Discuss.* **238**, 295–319 (2022).
42. A. L. Koritzke, N. S. Dewey, M. G. Christianson, S. Hartness, A. C. Doner, A. R. Webb, B. Rotavera, Probing O2-dependence of tetrahydrofuranyl reactions via isomer-resolved speciation. *Combust. Flame* **257**, 112640 (2023).
43. F. Bianchi, T. Kurtén, M. Riva, C. Mohr, M. P. Rissanen, P. Roldin, T. Berndt, J. D. Crounse, P. O. Wennberg, T. F. Mentel, J. Wildt, H. Junninen, T. Jokinen, M. Kulmala, D. R. Worsnop, J. A. Thornton, N. Donahue, H. G. Kjaergaard, M. Ehn, Highly oxygenated organic molecules (HOM) from gas-phase autoxidation involving peroxy radicals: A key contributor to atmospheric aerosol. *Chem. Rev.* **119**, 3472–3509 (2019).
44. S. W. Hartness, N. S. Dewey, M. G. Christianson, A. L. Koritzke, A. C. Doner, A. R. Webb, B. Rotavera, Probing O_2 dependence of hydroperoxy-butyl reactions via isomer-resolved speciation. *Proc. Combust. Inst.* **39**, 405–415 (2022).
45. N. Belhadj, M. Lailliau, R. Benoit, P. Dagaut, Experimental and kinetic modeling study of n-hexane oxidation. Detection of complex low-temperature products using high-resolution mass spectrometry. *Combust. Flame* **233**, 111581 (2021).
46. N. M. Donahue, S. Epstein, S. N. Pandis, A. L. Robinson, A two-dimensional volatility basis set: 1. Organic-aerosol mixing thermodynamics. *Atmos Chem Phys.* **11**, 3303–3318 (2011).
47. E. Trump, N. Donahue, Oligomer formation within secondary organic aerosols: Equilibrium and dynamic considerations. *Atmos. Chem. Phys.* **14**, 3691–3701 (2014).
48. D. R. Gentner, S. H. Jathar, T. D. Gordon, R. Bahreini, D. A. Day, I. E. Haddad, P. L. Hayes, S. M. Pieber, S. M. Platt, J. de Gouw, A. H. Goldstein, R. A. Harley, J. L. Jimenez, A. S. H. Prévôt, A. L. Robinson, Review of urban secondary organic aerosol formation from gasoline and diesel motor vehicle emissions. *Environ. Sci. Technol.* **51**, 1074–1093 (2017).
49. M. S. Reiter, K. M. Kockelman, The problem of cold starts: A closer look at mobile source emissions levels. *Transp. Res. D Transp. Environ.* **43**, 123–132 (2016).
50. A. K. Agarwal, A. P. Singh, R. K. Maurya, Evolution, challenges and path forward for low temperature combustion engines. *Prog. Energy Combust. Sci.* **61**, 1–56 (2017).
51. M. Moses-DeBusk, S. J. Curran, S. A. Lewis, R. M. Connatser, J. M. Storey, Impacts of air-fuel stratification in ACI combustion on particulate matter and gaseous emissions. *Emiss. Control Sci. Technol.* **5**, 225–237 (2019).
52. G. Lucachick, S. Curran, J. Storey, V. Prikhodko, W. F. Northrop, Volatility characterization of nanoparticles from single and dual-fuel low temperature combustion in compression ignition engines. *Aerosol Sci. Tech.* **50**, 436–447 (2016).

53. R. Volkamer, J. L. Jimenez, F. San Martini, K. Dzepina, Q. Zhang, D. Salcedo, L. T. Molina, D. R. Worsnop, M. J. Molina, Secondary organic aerosol formation from anthropogenic air pollution: Rapid and higher than expected. *Geophys. Res. Lett.* **33**, L17811 (2006).
54. K. S. Docherty, E. A. Stone, I. M. Ulbrich, P. F. DeCarlo, D. C. Snyder, J. J. Schauer, R. E. Peltier, R. J. Weber, S. M. Murphy, J. H. Seinfeld, Apportionment of primary and secondary organic aerosols in Southern California during the 2005 study of organic aerosols in riverside (SOAR-1). *Environ. Sci. Technol.* **42**, 7655–7662 (2008).
55. C. D. Cappa, S. H. Jathar, M. J. Kleeman, K. S. Docherty, J. L. Jimenez, J. H. Seinfeld, A. S. Wexler, Simulating secondary organic aerosol in a regional air quality model using the statistical oxidation model–Part 2: Assessing the influence of vapor wall losses. *Atmos. Chem. Phys.* **16**, 3041–3059 (2016).
56. A. Akherati, C. D. Cappa, M. J. Kleeman, K. S. Docherty, J. L. Jimenez, S. M. Griffith, S. Dusanter, P. S. Stevens, S. H. Jathar, Simulating secondary organic aerosol in a regional air quality model using the statistical oxidation model–Part 3: Assessing the influence of semi-volatile and intermediate-volatility organic compounds and NO_x. *Atmos. Chem. Phys.* **19**, 4561–4594 (2019).
57. J. Ensberg, P. Hayes, J. Jimenez, J. Gilman, W. Kuster, J. De Gouw, J. Holloway, T. Gordon, S. Jathar, A. Robinson, J. H. Seinfeld, Emission factor ratios, SOA mass yields, and the impact of vehicular emissions on SOA formation. *Atmos. Chem. Phys.* **14**, 2383–2397 (2014).
58. Y. Zhao, R. Saleh, G. Saliba, A. A. Presto, T. D. Gordon, G. T. Drozd, A. H. Goldstein, N. M. Donahue, A. L. Robinson, Reducing secondary organic aerosol formation from gasoline vehicle exhaust. *Proc. Natl. Acad. Sci. U. S. A.* **114**, 6984–6989 (2017).
59. K. Kohse-Höinghaus, Combustion, chemistry, and carbon neutrality. *Chem. Rev.* **123**, 5139–5219 (2023).
60. Z. Cheng, K. Atwi, O. E. Hajj, I. Ijeli, D. A. Fischer, G. Smith, R. Saleh, Discrepancies between brown carbon light-absorption properties retrieved from online and offline measurements. *Aerosol Sci. Tech.* **55**, 92–103 (2021).
61. Z. Cheng, K. Atwi, T. Onyima, R. Saleh, Investigating the dependence of light-absorption properties of combustion carbonaceous aerosols on combustion conditions. *Aerosol Sci. Tech.* **53**, 419–434 (2019).
62. Z. Cheng, K. M. Atwi, Z. Yu, A. Avery, E. C. Fortner, L. Williams, F. Majluf, J. E. Krechmer, A. T. Lambe, R. Saleh, Evolution of the light-absorption properties of combustion brown carbon aerosols following reaction with nitrate radicals. *Aerosol Sci. Tech.* **54**, 849–863 (2020).
63. P. H. McMurry, X. Wang, K. Park, K. Ehara, The relationship between mass and mobility for atmospheric particles: A new technique for measuring particle density. *Aerosol Sci. Technol.* **36**, 227–238 (2002).
64. G. S. Jatana, F. D. F. Chuahy, J. Szybist, The effect of spark-plug heat dispersal range and exhaust valve opening timing on cold-start emissions and cycle-to-cycle variability. *SAE Int. J. Adv. & Curr. Prac. in Mobility* **4**, 462–471 (2022).
65. G. S. Jatana, F. D. F. Chuahy, J. Szybist, "Effect of split-Injection strategies on engine performance and emissions under cold-start operation" (SAE Technical Paper No. 2023-01-0236, 2023).
66. S. Curran, J. Szybist, B. Kaul, J. Easter, S. Sluder, Fuel stratification effects on gasoline compression ignition with a regular-grade gasoline on a single-cylinder medium-duty diesel engine at low load. *SAE Int. J. Adv. & Curr. Prac. in Mobility* **4**, 488–501 (2022).
67. Y. Park, M. Moses-DeBusk, S. S. Sluder, S. P. Huff, Impact of biofuel blending on hydrocarbon speciation and particulate matter from a medium-duty multimode combustion strategy. *Energies* **16**, 5735 (2023).
68. A. Faccinetto, P. Desgroux, M. Ziskind, E. Therssen, C. Focsa, High-sensitivity detection of polycyclic aromatic hydrocarbons adsorbed onto soot particles using laser desorption/laser ionization/time-of-flight mass spectrometry: An approach to studying the soot inception process in low-pressure flames. *Combust. Flame* **158**, 227–239 (2011).
69. B. Apicella, A. Carpentieri, M. Alfè, R. Barbella, A. Tregrossi, P. Pucci, A. Ciajolo, Mass spectrometric analysis of large PAH in a fuel-rich ethylene flame. *Proc. Combust. Inst.* **31**, 547–553 (2007).
70. C. Russo, F. Stanzione, A. Ciajolo, A. Tregrossi, Study on the contribution of different molecular weight species to the absorption UV–Visible spectra of flame-formed carbon species. *Proc. Combust. Inst.* **34**, 3661–3668 (2013).
71. B. Apicella, C. Russo, A. Carpentieri, A. Tregrossi, A. Ciajolo, PAHs and fullerenes as structural and compositional motifs tracing and distinguishing organic carbon from soot. *Fuel* **309**, 122356 (2022).
72. A. P. Bateman, J. Laskin, A. Laskin, S. A. Nizkorodov, Applications of high-resolution electrospray ionization mass spectrometry to measurements of average oxygen to carbon ratios in secondary organic aerosols. *Environ. Sci. Technol.* **46**, 8315–8324 (2012).
73. P. Lin, P. K. Aiona, Y. Li, M. Shiraiwa, J. Laskin, S. A. Nizkorodov, A. Laskin, Molecular characterization of brown carbon in biomass burning aerosol particles. *Environ. Sci. Technol.* **50**, 11815–11824 (2016).
74. P. Lin, L. T. Fleming, S. A. Nizkorodov, J. Laskin, A. Laskin, Comprehensive molecular characterization of atmospheric brown carbon by high resolution mass spectrometry with electrospray and atmospheric pressure photoionization. *Anal. Chem.* **90**, 12493–12502 (2018).
75. A. P. Bateman, S. A. Nizkorodov, J. Laskin, A. Laskin, High-resolution electrospray ionization mass spectrometry analysis of water-soluble organic aerosols collected with a particle into liquid sampler. *Anal. Chem.* **82**, 8010–8016 (2010).
76. S. H. Budisulistiorini, M. Riva, M. Williams, J. Chen, M. Itoh, J. D. Surratt, M. Kuwata, Light-absorbing brown carbon aerosol constituents from combustion of Indonesian peat and biomass. *Environ. Sci. Technol.* **51**, 4415–4423 (2017).
77. C. M. Kenseth, N. J. Hafeman, Y. Huang, N. F. Dalleska, B. M. Stoltz, J. H. Seinfeld, Synthesis of carboxylic acid and dimer ester surrogates to constrain the abundance and distribution of molecular products in α-pinene and β-pinene secondary organic aerosol. *Environ. Sci. Technol.* **54**, 12829–12839 (2020).
78. R. Zhao, C. M. Kenseth, Y. Huang, N. F. Dalleska, J. H. Seinfeld, Iodometry-assisted liquid chromatography electrospray ionization mass spectrometry for analysis of organic peroxides: An application to atmospheric secondary organic aerosol. *Environ. Sci. Technol.* **52**, 2108–2117 (2018).
79. A. P. Bateman, M. L. Walser, Y. Desyaterik, J. Laskin, A. Laskin, S. A. Nizkorodov, The effect of solvent on the analysis of secondary organic aerosol using electrospray ionization mass spectrometry. *Environ. Sci. Technol.* **42**, 7341–7346 (2008).
80. M. Teich, D. van Pinxteren, M. Wang, S. Kecorius, Z. Wang, T. Müller, G. Mőnik, H. Herrmann, Contributions of nitrated aromatic compounds to the light absorption of water-soluble and particulate brown carbon in different atmospheric environments in Germany and China. *Atmos. Chem. Phys.* **17**, 1653–1672 (2017).
81. Z. Kitanovski, I. Grgić, R. Vermeylen, M. Claeys, W. Maenhaut, Liquid chromatography tandem mass spectrometry method for characterization of monoaromatic nitro-compounds in atmospheric particulate matter. *J. Chromatogr. A* **1268**, 35–43 (2012).
82. Y. Cheng, K.-b. He, Z.-y. Du, G. Engling, J.-m. Liu, Y.-l. Ma, M. Zheng, R. J. Weber, The characteristics of brown carbon aerosol during winter in Beijing. *Atmos. Environ.* **127**, 355–364 (2016).
83. J. Liu, M. Bergin, H. Guo, L. King, N. Kotra, E. Edgerton, R. Weber, Size-resolved measurements of brown carbon in water and methanol extracts and estimates of their contribution to ambient fine-particle light absorption. *Atmos. Chem. Phys.* **13**, 12389–12404 (2013).
84. S. K. Schum, L. E. Brown, L. R. Mazzoleni, MFAssignR: Molecular formula assignment software for ultrahigh resolution mass spectrometry analysis of environmental complex mixtures. *Environ. Res.* **191**, 110114 (2020).
85. G. W. Vandergrift, W. Kew, J. K. Lukowski, A. Bhattacharjee, A. V. Liyu, E. A. Shank, L. Paša-Tolić, V. Prabhakaran, C. R. Anderton, Imaging and direct sampling capabilities of nanospray desorption electrospray ionization with absorption-mode 21 Tesla Fourier transform ion cyclotron resonance mass spectrometry. *Anal. Chem.* **94**, 3629–3636 (2022).
86. G. W. Vandergrift, A. S. M. Shawon, D. N. Dexheimer, M. A. Zawadowicz, F. Mei, S. China, Molecular characterization of organosulfate-dominated aerosols over agricultural fields from the southern great plains by high-resolution mass spectrometry. *ACS Earth Space Chem.* **6**, 1733–1741 (2022).
87. R. T. Kelly, J. S. Page, Q. Luo, R. J. Moore, D. J. Orton, K. Tang, R. D. Smith, Chemically etched open tubular and monolithic emitters for nanoelectrospray ionization mass spectrometry. *Anal. Chem.* **78**, 7796–7801 (2006).
88. N. M. Donahue, A. Robinson, C. Stanier, S. Pandis, Coupled partitioning, dilution, and chemical aging of semivolatile organics. *Environ. Sci. Technol.* **40**, 2635–2643 (2006).
89. Y. Li, U. Pöschl, M. Shiraiwa, Molecular corridors and parameterizations of volatility in the chemical evolution of organic aerosols. *Atmos. Chem. Phys.* **16**, 3327–3344 (2016).
90. S. A. Epstein, I. Riipinen, N. M. Donahue, A semiempirical correlation between enthalpy of vaporization and saturation concentration for organic aerosol. *Environ. Sci. Technol.* **44**, 743–748 (2010).
91. A. C. Doner, J. Zádor, B. Rotavera, Unimolecular reactions of 2,4-dimethyloxetanyl radicals. *J. Phys. Chem. A* **127**, 2591–2600 (2023).
92. N. S. Dewey, B. Rotavera, Reaction mechanisms of alkyloxiranes for combustion modeling. *Combust. Flame* **252**, 112753 (2023).
93. H. J. Curran, P. Gaffuri, W. J. Pitz, C. K. Westbrook, A comprehensive modeling study of n-heptane oxidation. *Combust. Flame* **114**, 149–177 (1998).

Acknowledgments: The CDC and PCCI samples were collected as part of the Co-Optimization of Fuels & Engines (Co-Optima) project sponsored by the U.S. DOE Office of Energy Efficiency and Renewable Energy, Office of Bioenergy Technologies, and Office of Vehicle Technologies. The cold-start samples were collected as part of the Partnership to Advance Combustion Engines Consortium sponsored by the U.S. DOE Office of Vehicle Technologies. We thank K. Stork, M. Weismiller, and G. Singh for support of this work and S. Huff and S. Sluder for operating the diesel engine. We thank the University of Georgia Proteomics and Mass

Spectrometry Core Facility for performing the LDI-MS and ESI-MS analyses. **Funding:** This work was supported by the National Science Foundation, Combustion and Fire Systems Program within the Division of Chemical, Bioengineering, Environmental, and Transport Systems under award CBET-2125064 (to R.S. and B.R.); Gas-Phase Chemical Physics program within the Division of Chemical Sciences, Geosciences and Biosciences, Office of Basic Energy Sciences (BES), U.S. DOE under award DE-SC0021337 (to B.R.); U.S. DOE Office of Science User Facility sponsored by the Biological and Environmental Research program under contract no. DE-AC05-76RL01830 (to G.W.V., Z.C., and S.C.); and National Institutes of Health award no. S10OD025118. **Author contributions:** Conceptualization: R.S., B.R., O.E.H., M.M.-D., and G.S.J. Methodology: R.S., B.R., O.E.H, M.M.-D., G.S.J, S.C., and G.W.V. Investigation: O.E.H., C.K.G., A.A., S.W.H., A.R.W., N.S.D., A.C. D., G.W.V., Z.C., M.M.-D., G.S.J., and Y.P. Visualization: R.S., B.R., O.E.H., and S.W.H. Funding acquisition: R.S. and B.R. Writing—original draft: O.E.H., R.S., B.R., and S.W.H. Writing—review and editing: O.E.H., R.S., B.R., S.W.H., G.W.V., Z.C., S.C., M.M.-D., G.S.J., and Y.P. **Competing interests:** The authors declare that they have no competing interests. **Data and materials availability:** All data needed to evaluate the conclusions in the paper are present in the paper and/or the Supplementary Materials.

Submitted 16 June 2023
Accepted 18 October 2023
Published 17 November 2023
10.1126/sciadv.adj2832

Science Advances

Alkylperoxy radicals are responsible for the formation of oxygenated primary organic aerosol

Omar El Hajj, Samuel W. Hartness, Gregory W. Vandergrift, Yensil Park, Chase K. Glenn, Anita Anosike, Annabelle R. Webb, Nicholas S. Dewey, Anna C. Doner, Zezhen Cheng, Gurneesh S. Jatana, Melanie Moses-DeBusk, Swarup China, Brandon Rotavera, and Rawad Saleh

Sci. Adv. **9** (46), eadj2832. DOI: 10.1126/sciadv.adj2832

Science Advances (ISSN 2375-2548) is published by the American Association for the Advancement of Science. 1200 New York Avenue NW, Washington, DC 20005. The title *Science Advances* is a registered trademark of AAAS.